Chapter

Perpendicular Magnetic Insulator Films for Spintronics

Laith Alahmed and Peng Li

Abstract

The recent progress in spintronics opens up new directions for novel device concepts and fundamental understandings. This is possible because of magnetic insulators (MIs), which have paved the way toward pure spin current-based spintronics. MIs with perpendicular anisotropy expand the horizon further, enabling new functionalities such as low-power spin-orbit torque switching, high-speed domain-wall motion, high-frequency spin-orbit torque oscillation, etc. In this chapter, we review recent progress in spintronic experiments using barium hexagonal ferrite $BaFe_{12}O_{19}$—a magnetic insulator with perpendicular anisotropy. These results lay the foundation for using MIs with perpendicular anisotropy as a medium to develop new energy-efficient pure spin current-based electronics.

Keywords: magnetic insulator, perpendicular anisotropy, spin current, spin-orbit torque, spintronics

1. Introduction

Spintronics, also known as spin electronics, is a newly emerging field of research that focuses on the spin degree of freedom of electrons rather than their charge. Charge current is a flow of electrons from one point to another under the influence of an electric field. In spintronics, spin current can propagate within the material. A pure spin current can be generated through effects such as the spin Hall effect (SHE), spin pumping, spin-wave propagation, etc. The pure spin currents consume much less energy than charge currents. This is because of the absence of charge flow that eliminates the power consumption needed for the electric field required to drive charge flow [1–3].

In spintronics, magnetization switching is of both fundamental interest and technological significance. One way to switch the magnetization of a ferromagnetic film is through the spin filtering effect. In this case, a spin-polarized electrical current will be generated. As the polarized electrons flow through the ferromagnetic film, they transfer angular momentum to the film and produce a spin-transfer torque to switch the film. This torque is called spin-transfer torque (STT). Magnetic random-access memory based on STT has already been commercialized in recent years.

The above-mentioned spin-torque switching, however, has a limit. The angular momentum transferred per unit charge in the applied current usually cannot exceed a quantum of spin ($\hbar/2$). Recent work demonstrates that one can exceed this limit by the use of spin-orbit torque (SOT). The demonstration generally takes a nonmagnetic heavy metal (HM)/ferromagnetic metal (FM) bilayered structure and

makes use of the spin-orbit coupling-produced SHE in the HM film to convert an in-plane charge current to a pure spin current that flows across the HM thickness. This produces spin accumulation at the HM/FM interface and therefore exerts a SOT on FM. In this case, each electron in the applied current can undergo multiple spin-flip scattering at the interface, therefore enabling more efficient switching than in the conventional spin-transfer torque case.

The ferromagnetic films used in most of the SOT studies were all conductive. A direct consequence is the severe shunting current in the ferromagnet layer, which not only limits the switching efficiency but also causes parasitic effects. For example, previous works have shown that interfacing a TI with a conductive FM film can result in a significant modification or even complete suppression of the topological surface states (TSSs) in the TI layer. In a TI/FM heterostructure, the TSSs may have been largely spoiled by the FM electrons. This means that many large spin-orbit torques observed in TI/FM structures may not be due to TSS. In this context, the use of MIs in an HM/MI heterostructure can effectively avoid the shunting current. Moreover, the TSSs in a TI/MI structure can be preserved except for the opening of a small gap at the Dirac point when strong coupling exists at the interface. This will enable the magnetization switching due to *bona fide* TSSs.

Magnetic insulators include a large class of materials, including spinels, garnets, and ferrites. They have a general chemical formula of $M(Fe_xO_y)$, where M is representing non-iron metallic elements. MIs have several advantages over magnetic metals for SOT device applications. First, in a heavy metal/MI heterostructure, the charge current only flows in the HM layer but not in the MI layer. In contrast, in an HM/magnetic metal structure, the charge current also flows in the FM, resulting in certain parasitic effects. When the HM layer is replaced by a topological insulator with high resistivity, the advantage of zero shunting currents in the MI film becomes particularly important. Moreover, interfacing a topological insulator (TI) with a conductive FM can result in a significant modification or even complete suppression of the topological surface states (TSSs) in the TI layer. The use of a magnetic insulator can effectively avoid the shunting current; TSSs in a TI/magnetic insulator (MI) structure can also be well preserved.

In the ferrite family, hexagonal ferrites have strong magnetocrystalline anisotropy. For example, M-type barium ferrite ($BaFe_{12}O_{19}$, noted as BaM) has an anisotropy field of 17 kOe. The perpendicular anisotropy in MI films originates from bulk intrinsic anisotropy rather than interfacial anisotropy [4]. This means that, when being used for actual devices, the BaM film has no constrains on the thickness. This is in strong contrast with the ferromagnetic metal counterpart (e.g., CoFeB/MgO) that often has to be very thin to realize interfacial perpendicular anisotropy. In addition, the magnetic damping is usually significantly lower in MIs than in FMs. For example, the intrinsic Gilbert damping constant in BaM materials is 7×10^{-4}, which is at least 10 times smaller than the value in permalloy [5]. This advantage is significant for spin-torque oscillator applications, where the current threshold for self-oscillations decreases with the damping, as well as for logic device applications that require low-damping, insulating spin channels.

This chapter reviews the main advances made in spintronic experiments with BaM over the past several years. Section 2 gives a brief introduction to BaM and discusses its crystalline structure, magnetic properties, and thin film growth techniques. This section serves to provide a background for the discussions in the following sections. Section 3 reviews the advances of spintronic experiments with BaM. Section 3.1 provides an overview of the related spintronic experiments. Section 3.2 discusses the generation of pure spin currents through the spin Seebeck effect and photo-spin-voltaic effect in the Pt/BaM structure. Section 3.3 discusses the spin-orbit torque-assisted switching in BaM. Section 3.4 discusses the use of

topological insulator/BaM heterostructure for magnetization switching. Finally, Section 3.5 provides an outlook in the field of BaM materials and devices.

2. Properties of barium ferrite thin films

2.1 Atomic structure of BaM thin films

BaM is a hexagonal ferrite, which consists of close-packed layers of oxygen ions. **Figure 1** shows a unit cell of BaM. The Ba^{2+} ion is large, as is the O^{2-} ion, and the barium always replaces oxygen somewhere in the oxygen lattice. The close-packed layers form six fundamental blocks, namely, S, S^*, R, R^*, T, and T^* [5–7]. The S block consists of close-packed oxygen layers stacking in an ABCABC … sequence. It has a cubic spinel arrangement with the <1 1 1 > axis along the vertical direction. There are two units of Fe_3O_4 without any barium ions in each S block. The R block comprises close-packed oxygen layers stacking in an ABAB … sequence. It has a hexagonal closest packed structure along the vertical axis. Each R block has a unit formula of $BaFe_6O_{11}$. The T block is made of four oxygen layers, with a barium ion replacing an oxygen ion in the middle two layers, which gives a unit formula of $Ba_2Fe_8O_{14}$. The S^*, R^*, and T^* blocks are 180° rotations around the c-axis from the S, R, and T blocks. BaM is built from the stacking of S, R, S^*, and R^* blocks.

Trivalent Fe^{3+} ions occupy tetrahedral and octahedral sites as well as one trigonal bipyramidal site. Different sites account for different spin orientations and Bohr magnetons (μ_B). For example, a tetrahedral site contributes $2\mu_B$, while an octahedral site contributes $4\mu_B$ with opposite spin orientations in the S block. In the end, S, S^*, R, and R^* blocks contribute $2\mu_B$ each, leading to a moment of $40\mu_B$ for each unit cell. This gives a saturation magnetization of ~4700 G in bulk BaM. BaM has a strong

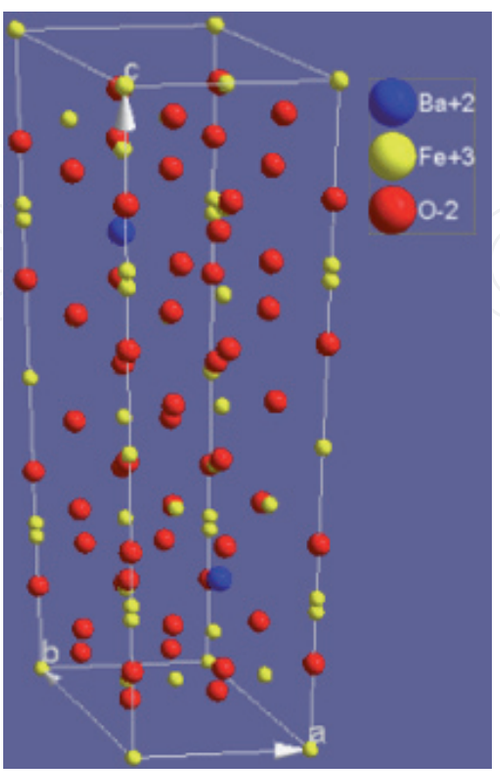

Figure 1.
Crystalline structure of M-type barium ferrite. Blue ball, Ba^{2+}. Yellow ball, Fe^{3+}. Red ball, O^{2-}.

anisotropy field of 17 kOe, which is along the *c* axis. This comes from the trigonal bipyramidal site Fe^{3+} ions, as well as breaking crystal symmetry in the R/R* blocks. This is the most distinguished property of BaM, because the perpendicular anisotropy field originates from bulk intrinsic anisotropy. BaM has a large *c* constant of 23.2 Å and an *a* constant of 5.89 Å. The *x*-ray density is about 5.29 g/cm^3. The Curie temperature of bulk BaM is 725 K, which is much higher than the room temperature. The exchange constant is 6.4×10^{-7} erg/cm [7].

2.2 Growth techniques

A variety of techniques are used to grow BaM thin films, including pulsed laser deposition (PLD) [8–10], alternating target laser ablation deposition (ARLAD) [11, 12], molecular beam epitaxy (MBE) [13], liquid phase epitaxy (LPE) [14, 15], magnetron sputtering [16, 17], and so on. Guo et al. at Boston Applied Technologies proposed a chemical solution deposition process to deposit BaM. Song and his colleagues succeeded in the PLD growth of BaM thin films that showed an FMR linewidth as narrow as single-crystal BaM bulks. However, these films showed a remanent magnetization much smaller than the saturation magnetization [9]. This problem was improved in the later experiments when tuning the deposition conditions [18]. **Figure 2** shows the PLD parameters which decide the thin film quality. **Figure 2b** shows that *c*-axis out-of-plane BaM grains can be grown on (0001) Al_2O_3 substrates; *c*-axis in-plane BaM grains can be grown on (11 −20) Al_2O_3 substrates. A typical procedure is as follows: the oxygen pressure is set at 300 mTorr, and the substrate is heated to 800°C. The substrate-to-target separation is fixed at 4 cm, and the energy fluence of the laser beam is set to 0.7 J/cm^2. The laser pulse repetition rate is increased from 1 to 5 pulse(s) per second in five equal steps over the first 5 min and is then set to 10 pulses/s for the remaining deposition. After the

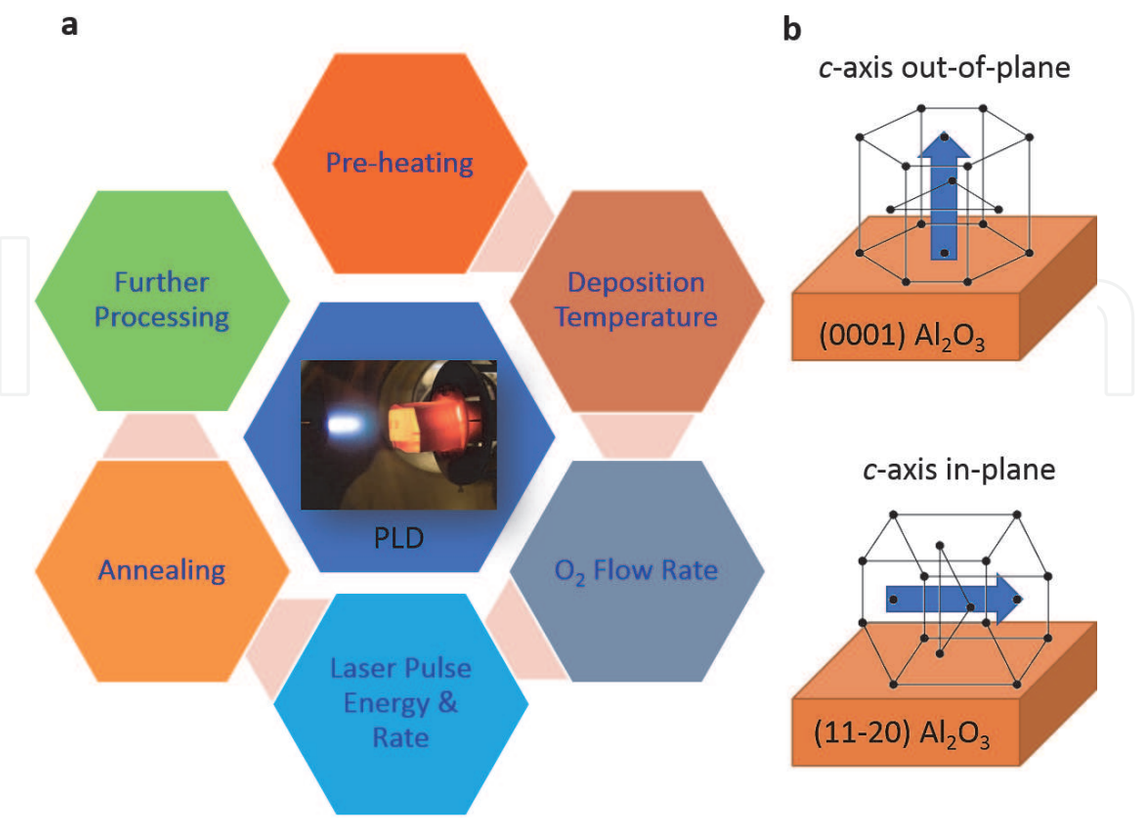

Figure 2.
Growth condition in pulsed laser deposition of BaM thin films. (a) Parameters controlling the BaM thin film quality. (b) Different Al_2O_3 substrate types for growing BaM with different c*-axis orientations.*

deposition, the substrate is cooled down at a rate of 2°C/min in 400 Torr oxygen. The sample is then annealed at 850°C for 4 h in a standalone tube furnace, with a heating rate of 10°C/min and a cooling rate of 2°C/min.

2.3 BaM thin film grown on (0001) *c*-plane Al_2O_3 substrate

In microwave device applications, BaM films usually have a thickness of several microns. For spintronic devices, the thickness is reduced to tens of nanometers. **Figure 3** shows the structure and magnetic properties of nanometer-thick BaM thin films grown on a *c*-axis Al_2O_3 substrate. The atomic force microscopy (AFM) image in **Figure 3a** shows a uniform and smooth surface, and the analysis of the AFM data yielded an RMS surface roughness of 0.19 ± 0.03 nm. These results, together with other AFM data not shown, indicate that the BaM film has a reasonably good surface, which is critical for the realization of high-quality BaM thin films. The roughness value here is an average over the measurements of nine different 1 × 1 μm areas, and the uncertainty is the corresponding standard deviation.

Figure 3b shows a $2\theta/\omega$ *x*-ray diffraction (XRD) scan, with the XRD intensity on a log scale. The *x*-ray θ rotation gave a scattered beam that matched the specular reflection from the surface. The detected (001) diffraction peaks all come from *c*-plane scattering of the BaM film. The (006) sapphire substrate peak was also detected. The hysteresis loops in **Figure 3c** were measured by a vibrating sample magnetometer with different field orientations, as indicated. The loops clearly show that the BaM film has perpendicular anisotropy, which confirms the *c*-axis orientation of the film. Analysis of the hysteresis data yielded an effective perpendicular anisotropy field around H_{ani} = 20 kOe, which is larger than the bulk value (17 kOe). The normalized saturation magnetization $4\pi M_s$ = 4.16 kG, which is lower than the bulk value of BaM (4.70 kG). **Figure 3d** presents a ferromagnetic resonance (FMR)

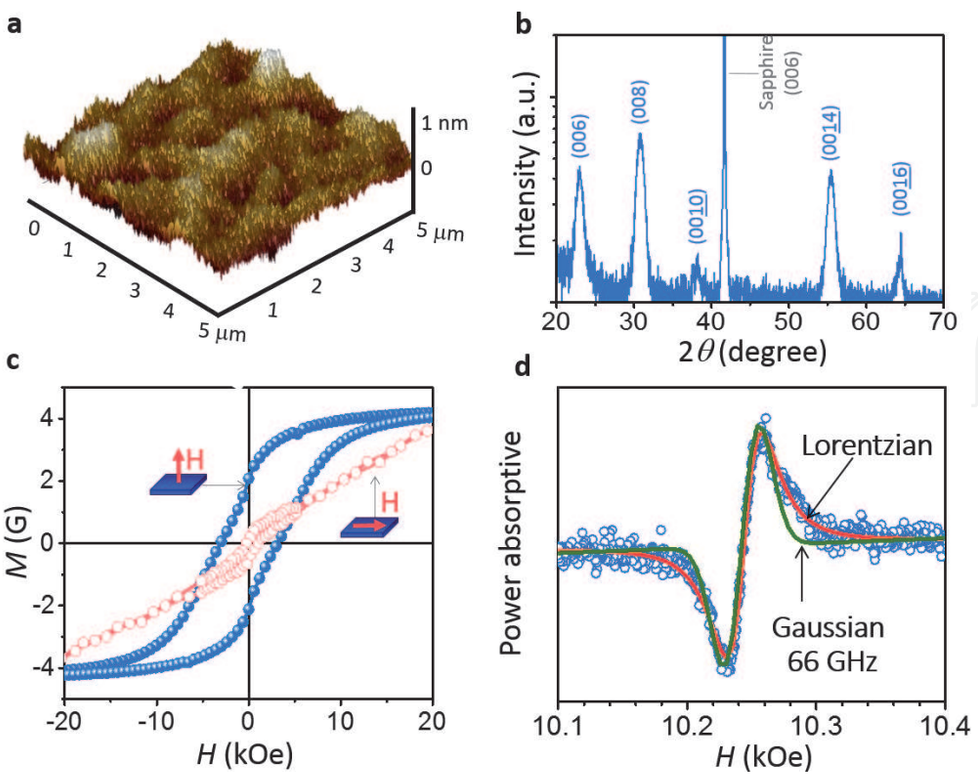

Figure 3.
Structure and magnetic properties of BaM thin films. (a) Atomic force microscope of 5 nm BaM thin film. (b) x-ray diffraction of 5 nm BaM thin film. (c) Hysteresis loops of 5 nm BaM thin film. Blue circles, H along out-of-plane direction. Red circles, H along in-plane direction. (d) Ferromagnetic resonance of 20 nm BaM thin film with H along out-of-plane direction. a, b, and c are adapted from [10].

curve obtained with a 20-nm-thick BaM film at ω = 66 GHz. Because of the strong perpendicular anistropy field, the ferromagnetic resonance of BaM film appears between 50 GHz and 75 GHz. In the graph, the blue circles show an FMR profile measured at 66 GHz. The Lorentzian function (red curve) fits the data points better than the Gaussian fit shown as the olive curve, indicating that the film has a uniform quality. The fitting yielded a peak-to-peak linewidth ΔH = 26.59 ± 0.60 Oe and an FMR resonance field H_{res} = 10.24 kOe. Similar measurements can be carried out to FMR profiles at a variety of frequencies, and a Kittel equation can fit the curve with a magnetic field applied out-of-plane:

$$\omega = 2\pi|\gamma|(H_{res} + H_{ani} - 4\pi M_s) \quad (1)$$

Such fitting yielded a gyromagnetic ratio γ = 2.80 ± 0.01 MHz/Oe and H_{ani} = 19.12 ± 0.04 kOe. The linewidth ΔH vs. frequency ω data can be fitted with the following equation:

$$\Delta H = \frac{2\alpha}{\sqrt{3}|\gamma|}\frac{\omega}{2\pi} + \Delta H_0 \quad (2)$$

where α is the damping constant and H_0 is the inhomogeneity line broadening, which is a parameter associated with α describing the damping of the material. The FMR measurements yielded a damping constant $\alpha = (9.7 \pm 1.1)\times 10^{-4}$.

2.4 BaM thin film grown on (1 1 −2 0) *a*-plane Al_2O_3 substrate

Figure 4 shows the structural and magnetic properties of a representative BaM film that is grown on an (1 1 −2 0) *a*-plane Al_2O_3 substrate. The film has a thickness

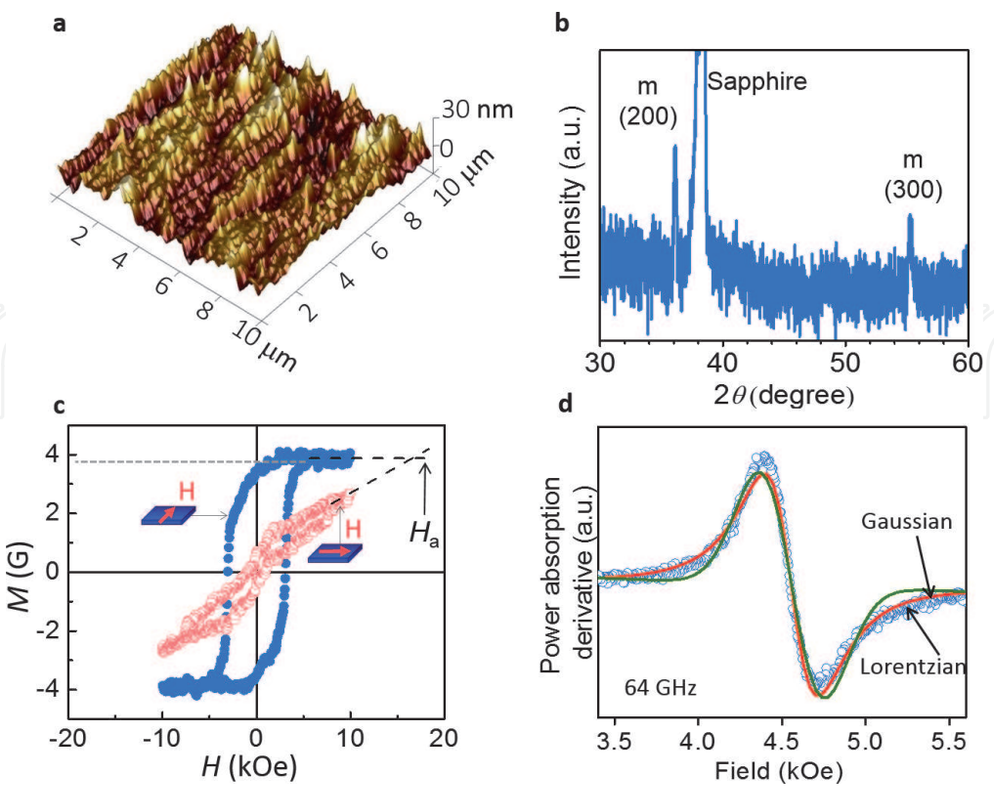

Figure 4.
Structure and magnetic properties of 1.2 μm BaM thin films with c-axis in plane. (a) AFM image. (b) XRD spectrum. (c) Hysteresis loops of the BaM thin film. Blue circles, H along the in-plane easy axis direction. Red circles, H along in-plane hard axis direction. (d) Ferromagnetic resonance spectrum with Gaussian and Lorentzian fittings. a, b, and c are adapted from [18].

of 1.2 μm. Thus, the AFM data show a relatively rough surface with an RMS surface roughness of 14.3 ± 1.6 nm. **Figure 4b** presents an XRD spectrum. The spectrum consists of a strong peak from the sapphire substrate and the two other peaks for the *m*-planes of the BaM film, indicating the in-plane orientation of the *c*-axis. **Figure 4c** presents the two hysteresis loops of the film measured by a vibrating sample magnetometer. One of the loops was measured with the magnetic field applied along the *c*-axis, while the other was measured with the field also in the film plane but perpendicular to the *c*-axis. The dashed lines indicate the extrapolations used to determine the effective anisotropy field H_{ani}. The dotted line indicates the determination of the saturation induction $4\pi M_{\text{s}}$. These data show that the film has a well-defined in-plane uniaxial anisotropy with the easy axis along the *c*-axis. From the hysteresis loops, it can be concluded that H_{ani} = 16.5 kOe and $4\pi M_{\text{s}}$ = 3.87 kG. Moreover, the film has a large remanent magnetization-to-saturation magnetization ratio of about 0.89 along the *c*-axis. This large ratio results from the strong in-plane uniaxial anisotropy. This means that the film is self-biased to a large degree at zero fields, which allows for the use of BaM in self-bias spintronic experiments. **Figure 4d** shows the FMR spectrum of the *c*-axis in-plane BaM film shown by the blue, open circles measured at 64 GHz. The curve is fitted to the derivatives of a trial Lorentzian function and a Gaussian function. Similar to the FMR curve in Section 2.3, it fits better with the Lorentzian function, indicating a uniform film. The Lorentzian fitting yields H_{res} = 4.55 kOe and ΔH = 318 Oe. The dependence of H_{ani} and the microwave frequency *f* can be fitted by a Kittel equation for field applied in-plane:

$$\omega = 2\pi|\gamma|\sqrt{(H_{\text{res}} + H_{\text{ani}})(H_{\text{res}} + H_{\text{ani}} + 4\pi M_s)} \tag{3}$$

3. Spintronic applications with magnetic insulators

3.1 Introduction to spintronics

In the following sections, we introduce recent spintronic experiments using MIs with strong anisotropy fields. Devices that incorporate the unique properties of MIs are an excellent potential solution for the power consumption and heat dissipation problems of conventional electronics, as they would consume much less energy and generate significantly less heat. We introduce the use of different techniques in generating pure spin currents, using bilayer heterostructures of a normal metal (NM)/ferromagnetic material. There are a variety of normal metal choices such as platinum (Pt) and Gold (Au). Both have been explored and tested in spintronics related studies and experiments [18–33].

In the first two sections, we will explore the generation of pure spin currents using the spin Seebeck effect (SSE) and the photo-spin-voltaic effect (PSVE). Both techniques take advantage of a NM coupled with a MI. In SSE, a temperature gradient in the MI is the main factor that induces the MI to inject pure spin currents into the NM layer. In PSVE however, the light of certain wavelengths reaching the atomic layers of the NM, exciting the NM electrons near the NM/MI interface, is what generates the pure spin currents. SSE and PSVE Experimentation results will also be explored and discussed. Then, in the last two sections, we will demonstrate how pure spin currents can be used practically to enhance magnetic switching in MIs in a significant and meaningful way. NM/MI bilayers will not be the only type of heterostructure discussed here, we will also explore topological insulator/MI structures and demonstrate the significance of topological insulators in spintronics.

3.2 Generation of pure spin currents through SSE using NM/BaM structures and photo-spin-voltaic effect in Pt/BaM structure

3.2.1 The spin Seebeck effect

The traditional Seebeck effect, first discovered by Thomas Seebeck in 1821 [34], refers to the generation of electric potential in a conductor when a temperature gradient is applied to it. The electric potential is caused by charge carriers within the conductor moving from the hot region to the cold region. A thermocouple consists of two dissimilar conductors that are joined to form a junction; when a heat gradient is applied across the thermocouple (see **Figure 5a**), a voltage difference can be observed across them. The sign of the voltage flips when the direction of the temperature gradient is flipped. The traditional Seebeck effect is the basic principle behind most thermoelectric generators.

The spintronic equivalent of the traditional Seebeck effect, called the spin Seebeck effect, was first discovered in 2008 [19, 28]. SSE is a phenomenon that can be observed in ferromagnetic and ferrimagnetic materials when a heat gradient is applied to them [19, 28, 35]. The heat gradient induces a spin voltage in the ferromagnet that can be used to inject pure spin currents into a conductor attached to the ferromagnet. Here, spin voltage is a potential for the spin of electrons, rather than their charge, to drive spin current [19, 36–38]. Previously mentioned bilayer heterostructures of normal metal/magnetic material have been used to study the SSE in two different configurations: transverse and longitudinal [19, 39]. In the transverse configuration, the generated spin current is perpendicular to the temperature gradient [28]. The generated spin current in the longitudinal configuration is parallel to the temperature gradient [19] (see **Figure 5b**). The longitudinal configuration has been the dominant choice for SSE research, owing to its simplicity [19]. Magnetic insulators (such as YIG, BaM, etc.) offer an ideal platform for observing the longitudinal spin Seebeck effect (LSSE) [19, 40]. In a conductive ferromagnet, the longitudinal configuration can give rise to a large anomalous Nernst effect (ANE)-induced voltage, which makes it difficult to distinguish between ANE and SSE [19, 33, 41, 42].

If SSE generates pure spin currents, then an important question would be how do we measure them? The absence of charge flow makes it impossible to use conventional methods to measure the spin currents. One way to measure LSSE-generated spin current is to first convert it into a charge current that can then be measured by conventional means. In this context, the choice of the normal metal in

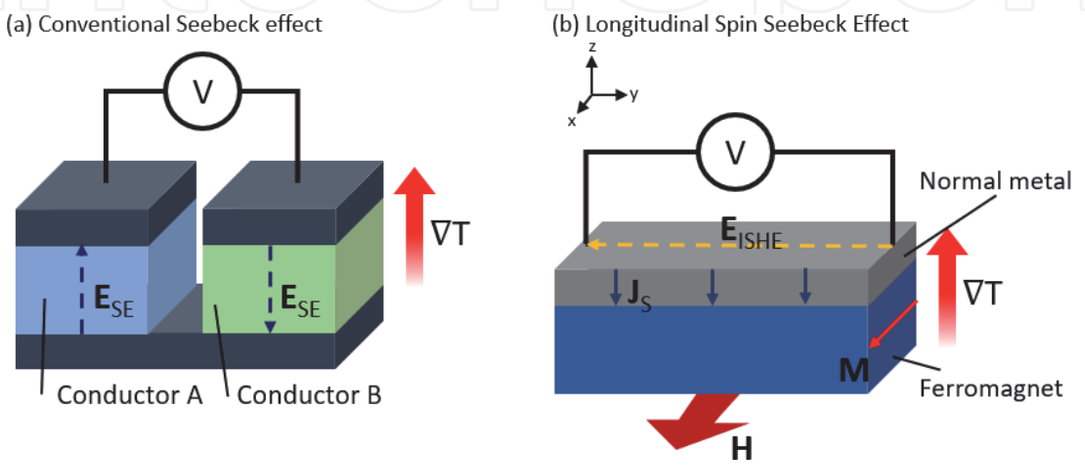

Figure 5.
Schematic illustrations of (a) the conventional Seebeck effect and (b) longitudinal spin Seebeck effect.

the bilayer heterostructure becomes very important. Heavy metals, such as Pt and Au, have strong spin-orbit coupling [43, 44], offering an effective mechanism to convert a transverse spin current into a longitudinal charge current through inverse spin Hall effect (ISHE) [43, 45–47]. The ISHE charge current across the heavy metal surface creates an electric field E_{ISHE} that can be measured with a voltmeter. The magnitude and sign of E_{ISHE} depend on internal and external factors. In **Figure 5b**, an external magnetic field H is applied in the x direction. The magnetization M of the MI layer is aligned to the x direction as well. The temperature gradient is applied across the z direction, generating a spin voltage in the MI layer, injecting spin current across the interface and into the normal metal layer parallel to the temperature gradient. The polarity of electron spins in the normal metal layer is influenced by M from the MI layer. The ISHE field, E_{ISHE}, is measured across the y direction. E_{ISHE} is proportional to the cross product of the spatial direction of the generated spin current J_s and the polarity vector of electron spins in the normal metal layer. The following equation explains the relationship between E_{ISHE}, J_s, and σ [19]:

$$E_{\mathrm{ISHE}} \propto J_s \times \sigma \tag{4}$$

In summary, the voltage measured across the normal metal surface is strongest when M is perpendicular to both the heat gradient and E_{ISHE}; the voltage will flip its sign if M is flipped by flipping the external magnetic field H; the voltage measured will be zero when M is parallel to E_{ISHE}.

This discussion sheds light on the importance of the existence of an external magnetic field H to enable E_{ISHE} when using soft magnetic insulators such as spinels and garnets. A strong enough H is necessary to saturate the magnetization of such insulators, as well as to control the direction of the magnetization. Indeed, SSE cannot be observed in samples incorporating spinels or garnets with a temperature gradient alone. Due to their low remnant magnetization, an appropriate external magnetic field is required to saturate them.

An exception to the external magnetic field requirement is made when using BaM thin films due to their strong uniaxial anisotropy [18]. In the absence of an external magnetic field, the magnetization of BaM films, caused by the spins of unpaired electrons, tend to favor one axis, called the easy axis, over any other axis. Thus, most electron spins within the BaM film tend to align themselves with the easy axis, randomly up or down, in the absence of an external magnetic field. Therefore, BaM films have uniaxial anisotropy. The uniaxial field of BaM was found to be around 16.5 kOe [9, 18]. Applying a magnetic field of this value or higher along the easy axis of the film causes all the electron spins to align themselves in the direction of the magnetic field, removing the magnetic field then will leave a large remnant magnetization within the BaM film owing to its uniaxial anisotropy. Namely, the film becomes self-biased and does not require an external field to magnetize it.

An LSSE experiment and its results using a Pt/BaM heterostructure [18] will be discussed next. In this experiment the sample consisted of a micron-thick BaM layer, topped with a 2.5-nm-thick Pt layer. The BaM layer was grown on a 0.5 mm sapphire substrate. The easy axis of the BaM film was in the plane of the film.

Figure 6 shows the experiment setup and results. **Figure 6a** shows a schematic diagram of the experimental setup that was used to test LSSE within the sample. The sample was put on an aluminum plate to act as a heat sink. An incandescent light bulb was placed directly on top of the sample, acting as the heat source. The easy axis of the BaM layer was along the y-axis, and the voltage was measured along the x-axis. All measurements were performed without an external magnetic field. However, a magnetic field of 10 kOe was used prior to the experiment to set the magnetization M of the BaM film in the positive (or negative) y direction.

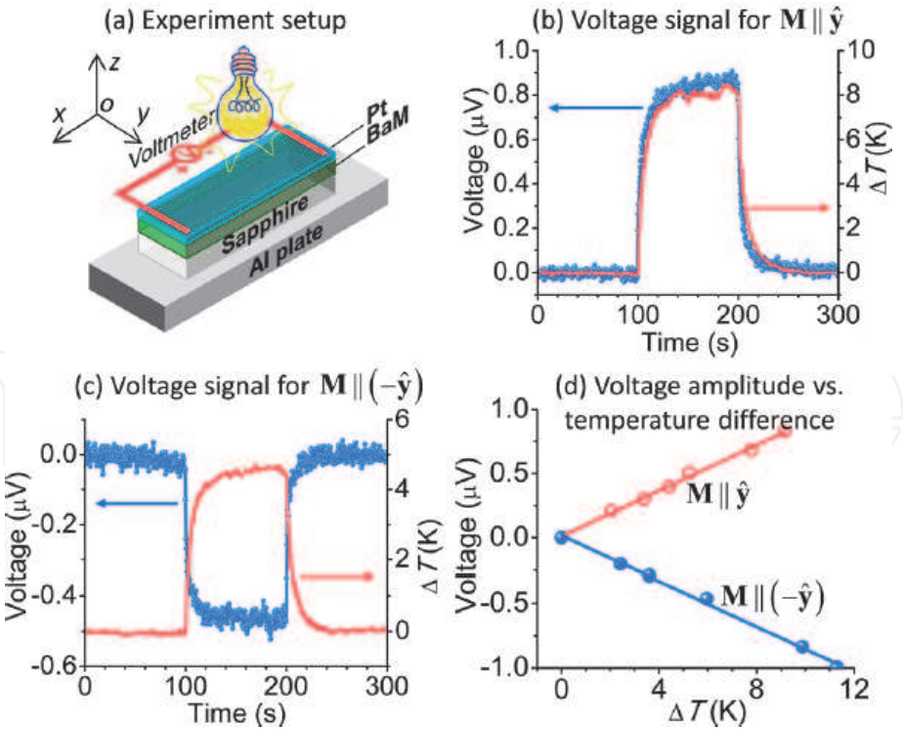

Figure 6.
Light-induced generation of spin currents. (a) The experimental setup. (b) and (c) Respective voltage signals measured for M||y and M||(−y), in response to the light that was turned on at 100s then turned off at 200s. The graphs also show the responses of the temperature difference (ΔT) between the top and bottom of the Pt/BaM/Saphire structure. (d) Voltage amplitude as a function of ΔT. Source: [18], p. 3.

The heat from the light bulb, along with the aluminum plate acting as a heat sink, created the temperature gradient across the BaM film thickness; the difference in temperature between the bottom surface and top surface of BaM, ΔT, was measured using two thermocouples connected to them. When the light is turned on, SSE occurs, the heat gradient induces a spin voltage in the BaM film that injects spin currents across the interface and into the Pt layer. Due to ISHE, the spin current is converted to a charge current across the Pt surface creating a voltage. The voltage was measured by connecting a nanovoltmeter to the opposite ends of the Pt surface across the x-axis.

Figures 6b and **c** demonstrate the relationship between the difference in temperatures ΔT and the generated voltage, with time, for $M\|y$ and $M\|{-y}$, respectively. ΔT was changed by changing the height of the light bulb. These results show that the SSE-generated spin current, and therefore the observed voltage, changes in exactly the same manner that ΔT changes with. This result is expected as the difference in temperature is what causes the spin voltage in the BaM film, which ultimately gives us the voltage reading across the Pt layer.

Figure 6d shows an important property of SSE, namely, the sign of the generated voltage flips when the direction of the BaM magnetization is flipped. The graph shows the relationship between ΔT and measured voltage for $M\|y$ (red) and $M\|{-y}$ (blue). The result again proves that the voltage change with respect to ΔT is identical (mirrored when $M\|{-y}$ due to the sign flip), in both cases.

Control measurements were performed and are shown in **Figure 7**. Changing the lateral position of the light bulb did not have any noticeable effect on the measured voltage. This is to be expected, as the temperature gradient depends on the height of the light bulb, rather than its lateral position. This is demonstrated in **Figure 7a**, where the light position was changed to six different lateral positions. The figure shows that, other than jumps from electrical disturbance caused by the position change, the measured voltage remained largely unchanged.

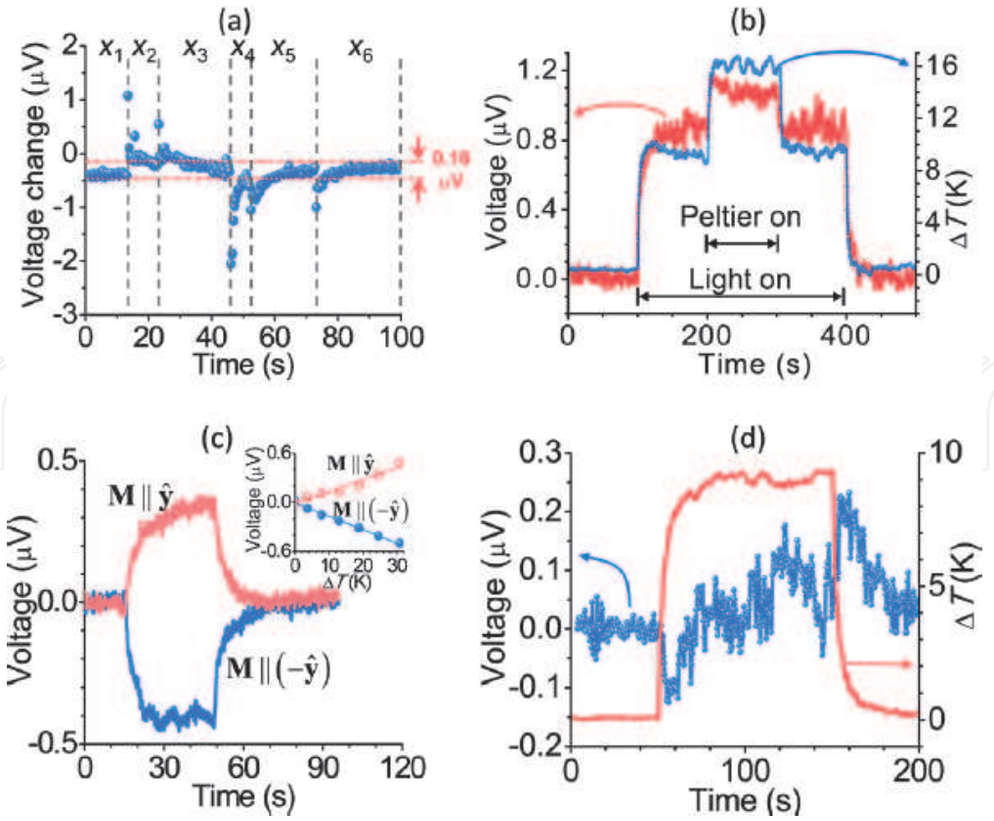

Figure 7.
Control measurements. (a) Voltage changes caused by moving the bulb along the x-axis. (b) Voltage and ΔT signals obtained when both a bulb and a Peltier cooler were used to control the temperature. The data in (a) and (b) were obtained with the same sample as ***Figure 6****. (c) SSE in a Pt(2.5 nm)/BaM(0.4 μm)/sapphire (0.5 mm) sample. (d) Voltage and ΔT signals obtained with a Cu(9 nm)/BaM(1.2 μm)/sapphire (0.5 mm) sample. Source: [18], p. 3.*

Using a Peltier cooler as an added source for the temperature gradient in addition to the light bulb also did not have a noticeable change in the relationship between the measured voltage and ΔT. This is shown in **Figure 7b**, where a light source was used to create ΔT, and a Peltier cooler was turned on under the sample midway through. **Figure 7c** shows the voltage change with time for a similar sample with a BaM layer thickness of 0.4 μm, and only a Peltier cooler was used to create the temperature gradient. Both **Figure 7b** and **c** show the same result: the measured voltage is directly related to ΔT, regardless of the method used to achieve ΔT.

The importance of using a metal with strong spin-orbit coupling is demonstrated through **Figure 7d**, where Cu, which has very weak spin-orbit coupling, and therefore very weak ISHE, was used in a Cu (9 nm)/BaM (1.2 μm)/sapphire (0.5 mm) sample. The figure shows a behavior that is different from the Pt/BaM samples, indicating the absence of SSE in this sample. A likely source for the signal shown in **Figure 7d** is the conventional Seebeck effect, caused by a temperature gradient across the sample's length. (All figures, experimentation setup and results were taken from [18] with appropriate permissions).

3.2.2 Photo-spin-voltaic effect

A closely related but fundamentally different effect to SSE is the photo-spin-voltaic effect (PSVE). PSVE happens in NM/MI heterostructures; it generates pure spin currents across the NM thickness that can be measured through ISHE. Light can generate spin voltage and drive spin currents through PSVE. While the spin voltage is generated in the MI layer in the SSE case, the spin voltage in PSVE is

generated in the atomic layers of the NM that are close to the interface due to magnetic proximity effect [48]. When light of a certain wavelength hits the sample, photons excite electrons in the Pt layer, causing them to move to higher energy bands. The efficiency of this photon-driven excitation varies because of the spin orientation. The difference in efficiency, along with different diffusion rates of excited electrons and holes, generates the spin voltage through PSVE [48].

Figure 8 shows PSVE in a Pt/MI structure. An important question arises due to the extremely similar setup of both LSSE and PSVE: how can we determine the source of the ISHE generated voltage? It could be due to LSSE, or PSVE, or both. Fortunately, research in this area determined several distinguishable factors that make it possible to disentangle LSSE from PSVE. The most important factor is the wavelength of the light used to excite the sample. Experimental results determined that PSVE can only be observed when the wavelength of the light used falls in the range 1600–2000 nm [48]. Using a light source with a wavelength outside that range or a heat source other than light, such as a Peltier cooler, will only give us LSSE in our sample and no PSVE [49]. Other factors include the type of materials and device geometries used in the studies. For example, different MI types and thicknesses give widely different signals in LSSE. A recent work showed that the main contribution in the voltage comes from LSSE rather than PSVE [50]. However, experiments have shown that using a light source with the appropriate wavelength gives extremely similar results in Pt that is coupled with MI of varying types and thicknesses [48].

Figure 9 shows the results of PSVE in three different samples: Pt (2.5 nm)/YIG (78 μm), Pt (2.5 nm)/YIG (21 nm), and Pt (2.5 nm)/BaM (1.2 μm). For each sample, three different experimental setup configurations were tested: illuminating from the sample's top, illuminating from the sample's bottom, and illuminating from both the top and bottom of the sample. The phenomena of PSVE in all cases were similar, with a difference that is no bigger than an order of magnitude. This confirms that the voltage is induced by PSVE instead of SEE. Only the sign of the voltage, but not its magnitude, flipped with the flipping of the magnetization of the MI film; this confirms the spin origin of the measured voltage. (All the PSVE information and experimental setup and discussion were taken from [48] with appropriate permissions).

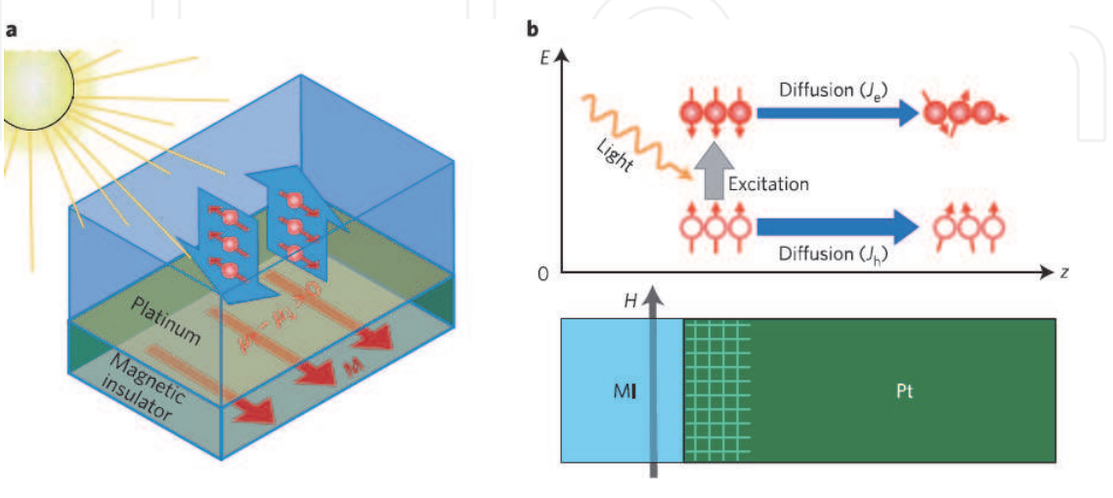

Figure 8.
(a) Photo-spin-voltaic effect in Pt/MI bilayer heterostructure. (b) Sketch of the physical mechanism underlying PSVE. When light illuminates the sample, photons excite electrons and generate nonequilibrium hot electrons and holes in the Pt atomic layers that are in proximity to the MI (the gridded region). The excited electrons and holes diffuse from Pt/MI interface to the Pt interface (along the +z direction), giving rise to spin currents (J_e and J_h). Source: [48], pp. 861, 865.

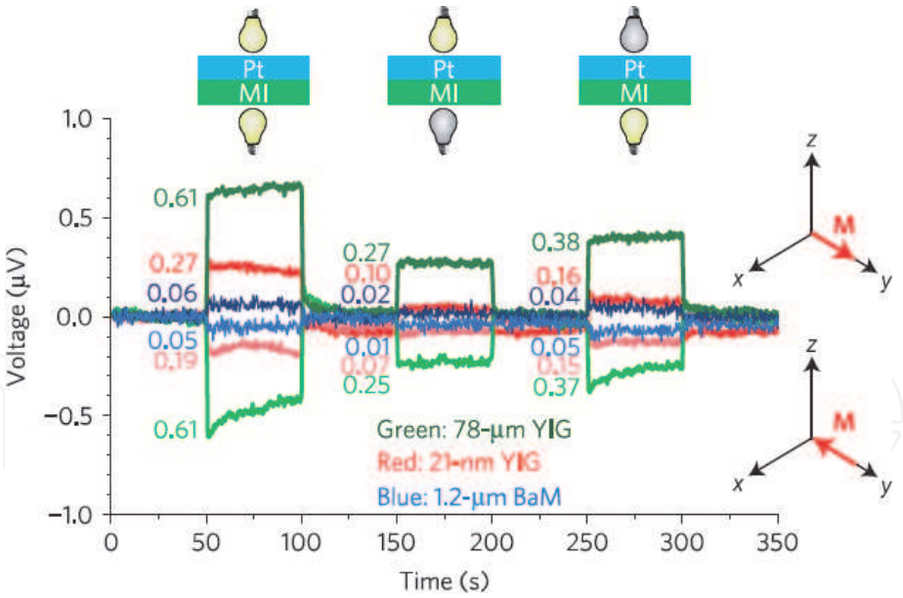

Figure 9.
Measurements for different illumination/magnetization configurations for three different samples Pt (2.5 nm)/YIG (78 μm), Pt (2.5 nm)/YIG (21 nm), and Pt (2.5 nm)/BaM (1.2 μm). Source: [48], p. 863.

3.3 Spin-orbit torque-assisted switching in magnetic insulators

The uniaxial anisotropy and the nonvolatile nature of easy axis-aligned magnetization within the BaM film can be used to design memory and logic-based systems. If the magnetization is up, it will keep its direction until a magnetic field flips it toward the opposite direction. If an efficient way can be found to switch the magnetization states of the magnetic insulator thin films, then they can be used in magnetic memory systems commercially [51].

In a NM/MI structure, such as Pt/BaM, SHE can be used to convert a charge current across the Pt surface into a spin current that flows across the thickness of Pt through spin-orbit coupling; this process will accumulate spins at the Pt/BaM interface. The spin accumulation generates spin-orbit torques (SOTs) that can be used to switch the BaM magnetization. Each electron provided by the charge current can undergo several spin-flip scatterings at the interface, breaking the conventional spin-torque switching limit and increasing the switching efficiency considerably [51].

We discuss the SOT experimental details of a Pt(5 nm)/BaM(3 nm) sample. The easy axis of the BaM film was perpendicular to the surface of the film. **Figure 10b** shows the hysteresis loop of the film, measured by a vibrating sample magnetometer, when an out-of-plane external magnetic field was applied (red curve). The olive curve shows the hysteresis loop along the hard axis when the external magnetic field is applied in the plane of the film. This figure confirms the perpendicular uniaxial anisotropy of the film, with a perpendicular anisotropy field of 17.6 kOe. A Hall bar structure was fabricated out of the Pt/BaM bilayer and is shown in **Figure 10a**. **Figure 10c** shows a hysteresis loop on the Hall resistance, revealing an anomalous Hall effect (AHE)-like behavior. It is unclear whether the AHE-like behavior is from magnetic proximity effect or spin Hall magnetoresistance. However, R_{AHE} behaves in a very similar manner to the perpendicular magnetization component of the BaM film $M_{\perp}$ (compare **Figure 10b** to **Figure 10c**). This allows for the gauging of $M_{\perp}$ in the BaM film by simply measuring R_{AHE}.

The first experiment demonstrated was the out-of-plane switching; the external magnetic field is fixed out of the film's plane and 20° off the easy axis. The purpose of this tilt was to break the magnetization symmetry due to the external field,

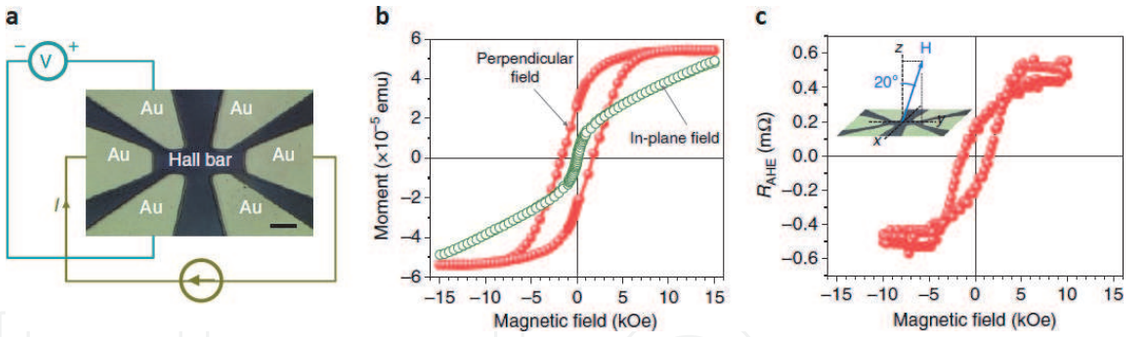

Figure 10.
(a) Optical image of the Pt (5 nm)/BaM (3 nm) Hall bar structure. (b) Magnetic hysteresis loops of the BaM film. (c) Anomalous Hall resistance R_{AHE} of the Hall bar measured as a function of a magnetic field. The inset is a schematic showing the magnetic field H direction which is in the yz plane and 20 degrees away from the +z axis. Source: [51], p. 3.

allowing for the observation of the SOT effect. One would expect that if the SOT field is along the *-z* direction, it would act against the external field, thereby increasing the total field required to saturate the magnetization within the BaM film, while a SOT field along the *z* direction will aid the external field, resulting in a smaller field required to saturate the magnetization of the BaM film.

Indeed, experimental results, shown in **Figure 11**, confirm exactly that. Namely, when charge currents of varying intensities are applied to the Pt film along the $-y$ direction, the SOT direction is opposite to that of H (as shown in **Figure 11a**), and the resultant hysteresis loops, gauged by R_{AHE}, become wider as the current intensity increases. This is shown in **Figure 11c**, where the gray loop is for $I = 0$; blue, $I = -2$ mA; olive, $I = -4$ mA; and red, $I = -6$ mA. This confirms the existence and

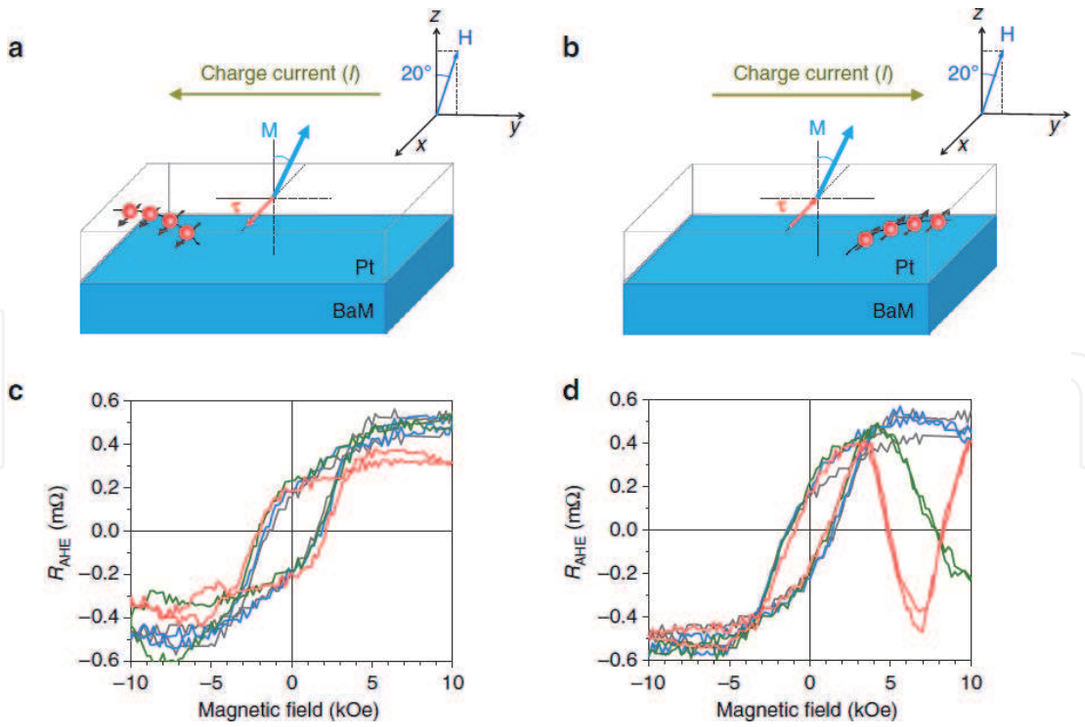

Figure 11.
Switching responses in Pt/BaM for out-of-plane magnetic fields. (a) and (b) Effects of charge currents I *in the Pt film on switching of the magnetization* M *in the BaM film under an out-of-plane field H. The red spheres with arrows represent spin-polarized electrons deflecting toward the BaM layer.* M *represents the magnetization of BaM. τ represents the spin torque due to SHE. The direction of* H *is indicated in the insert. (c) and (d) Anomalous Hall resistance* R_{AHE} *of the Hall bar measured as a function of a magnetic field for different charge currents. The field was applied 20 degrees away from the z axis, as shown in the insets of (a) and (b). In (c) gray,* I = 0*; blue,* I = −2 *mA; olive,* I = −4 *mA; and red,* I = −6 *mA. In (d) gray,* I = 0*; blue,* I = 2 *mA; olive,* I = 4*mA; and red,* I = 6 *mA. Source: [51], p. 4.*

the direction of pure spin current-generated SOTs near the interface, the magnitude of which is proportional to the intensity of the supplied current. Flipping the direction of the supplied charge currents flips the direction of the SOT as shown in **Figure 11b**. The resultant hysteresis loops, shown in **Figure 11d**, become narrower as the supplied charge current increases, indicating that SOT, in the direction of H, assisted in the magnetization flipping, reducing the overall total external field needed to flip $M_\perp$ in the BaM film.

Further experiments were performed to confirm the existence of spin current-generated SOT near the Pt/BaM interface. This time, the external field H was within the film plane. This means that applying a saturation field in the film plane will align the electron spins along the hard axis of the BaM film. When H is removed, the spins will return to their easy axis, randomly up or down, resulting in a net $M_\perp$ of zero. However, when a charge current is supplied to the Pt surface, SOT near the interface will influence the direction of the spins of electrons when H is reduced and they start to align to their easy axis. This results in remnant magnetization that is represented by a hysteresis loop. If the direction of the supplied charge current is flipped, the resultant hysteresis loop will be the opposite of the first hysteresis loop. This is shown in **Figure 12**. This confirms that the direction of the SOT can be controlled by changing the sign of the supplied charge current.

These results confirm that SOT due to pure spin currents, generated by SHE in Pt/BaM structures, can be used to assist the magnetization switching in BaM films. It should be noted however, that SHE generates two different torques: a damping-like torque (DLT) and a field-like torque (FLT). The effective fields for DLT and FLT are H_{DLT} and H_{FLT}, respectively. Thus, the total field affecting $M_\perp$ of the BaM film can be written as follows [51]:

$$H_{total} = H + H_a + H_{FLT}x + H_{DLT}(m \times x) \tag{5}$$

where H is the external field as indicated in **Figure 11**, H_a is the anisotropy field of the BaM film, and x is the unit vector along the $+x$ direction. Two different simulation models were carried out to determine the SOT field strength: macrospin model simulation and microspin model simulation.

Carrying out both simulations involved three main steps: first, H_c was calculated when J_c is set to zero. H_{DLT} and H_{FLT} were both set to zero as well. H_a was set such that when H is equal to the experimentally measured H_c and pointing in the direction opposite to its initial direction, m flips. The second step considers the case when

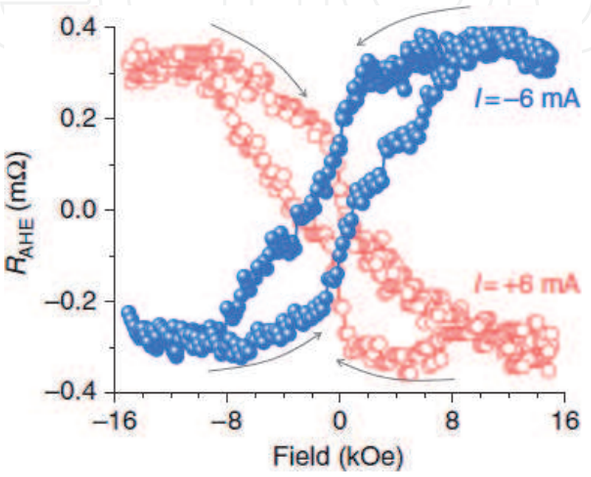

Figure 12.
Anomalous Hall resistance R_{AHE} measured as a function of a magnetic field along the y *axis for* I= *+6 mA and* I= *−6 mA, respectively. Source: [51], p. 5.*

$J_c \neq 0$ and $H_{FLT} = 0$. Simulations are then performed at given H_{DLT} values to find the corresponding H_c values. This is because a flip in the direction of H_{DLT} breaks the symmetry, thereby affecting H_c. A flip in the direction of H_{FLT} on the other hand does not affect H_c as H_{FLT} is orthogonal to H_a, H, and m. The third step considers non-zero values of H_{DLT} and repeats the simulations to find H_c for given combinations of H_{DLT} and H_{FLT} values.

The results from running the two different models of simulations were very close and are shown in **Figure 13**. The blue dots show the linear nature of the relationship between H_c and H_{DLT}, when $H_{FLT} = 0$. This is similar to the experimental H_c vs. J_c data. The simulation showed that when H_{DLT} is -400 Oe, H_c increases to about 2.0 kOe, and when H_{DLT} is 400 Oe, H_c decreases to about 0.95 kOe. This same change was experimentally observed when J_c changed between -10^7 A cm^{-2} and 10^7 A cm^{-2}. Thus, we can conclude that H_{DLT} in the Pt/BaM is about 400 Oe at $J_c = 10^7$ A cm^{-2}. The red and olive dots in **Figure 13a** and **b** show the same relationship when $H_{FLT} = H_{DLT}/2$ and $H_{FLT} = H_{DLT}$, respectively. The red dots show that the effect of H_{FLT} is negligible when $H_{FLT} = H_{DLT}/2$, while the olive dots show a deviation for strong negative charge currents that was not observed experimentally. The red and olive portions of both figures prove that the majority of the SHE generated torque is due to DLT, with FLT having a relatively small effect in comparison. The experimental results, along with the simulation data, show that SOT in Pt/BaM films can reduce the required switching field by as much as 500 Oe.

Further improvements and enhancements in the switching efficiency can be achieved by using materials with higher spin-orbit coupling, resulting in stronger SOT. Topological insulators exhibit such requirements and will be the topic of the next section. (All figures, experimentation setup, and results were taken from [51] with appropriate permissions).

3.4 Magnetization switching with topological insulators

Topological insulators (TI) are of great interest in spintronic-related studies. A TI is a material with nontrivial symmetry-protected topological order that behaves as an insulator in its interior but whose surface contains conducting states. What differentiates a TI from other materials with conducting surfaces is that its surface

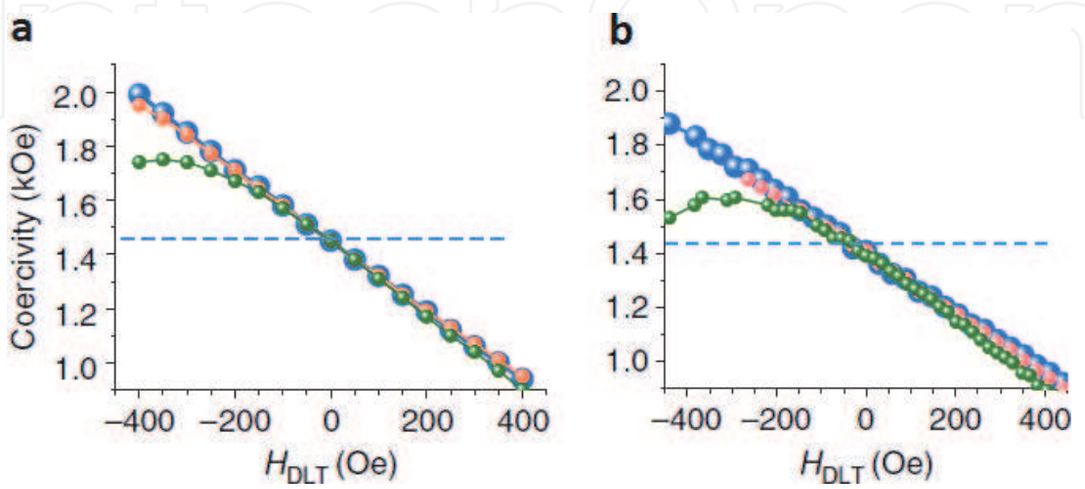

Figure 13.
(a) and (b) Coercivity vs. DLT field (H_{DLT}) estimated for three different field-like torque (FLT) fields (H_{FLT}) through macrospin and full micromagnetic simulations, respectively. Large blue spheres, $H_{FLT} = 0$; small red spheres, $H_{FLT} = H_{DLT}/2$; and small olive spheres, $H_{FLT} = H_{DLT}$. The dash line in (a) and (b) is the H_c at $I = 0$. All the measurements were done at room temperature. Source: [51], p. 4.

states are time-reversal symmetry-protected. Due to the very strong spin-orbit coupling of TIs [10, 52], if a charge current is supplied to their surface, the surface states induce spin polarity and therefore generate a spin current, owing to the SHE. The SHE in TIs is several times stronger than in heavy metals such as Pt, and it can become hundreds of times stronger at very lower temperatures [10].

Theoretically, the very strong SHE in a TI can generate SOT that is much stronger than its counterpart in heavy metals. This strong SOT can then be exploited for magnetization switching by pairing it with a ferromagnet, similar to what was discussed in the previous section. Using a conductive ferromagnet, however, can completely suppress the surface states of a TI [49–56], preventing the generation of spin currents, therefore making it impossible for SOT magnetization switching to happen in TI/conductive ferromagnet structures.

Here, the usefulness and importance of magnetic insulators are again emphasized. Pairing a TI with MI keeps the integrity of the surface states. Various materials can be used to create a TI, such as $(Bi_xSb_{1-x})_2 Te_3$. The choice of x can ensure protection from time-reversal symmetry. **Figure 14a** and **b** show the sheet resistance measurements of a $(Bi_xSb_{1-x})_2Te_3$ film that was grown on a MI ($Tm_3Fe_5O_{12}$, TIG) for $x = 0.2$ and $x = 0.3$, respectively. The lower inset of both figures show the broken symmetry of the topological surface states of both configurations. The sheet resistance in both figures shows a linear portion, attributed to the normal Hall effect, and a hysteresis loop portion. The different slopes indicate opposite carriers in each sample. The hysteresis portion indicates strong magnetic uniaxial anisotropy in the TI owing to highly spin-polarized electrons on the TI's surface. This uniaxial anisotropy is maintained at room temperature and up to T = 400 K [57].

In another experiment, the authors used a Bi_2Se_3/BaM heterostructure to explore the effect of topological surface state in switching the magnetization of a magnetic insulator [10]. The BaM layer used had similar characteristics to the BaM layer used in the Pt/BaM experiment. The BaM film was 5-nm-thick and had a uniaxial anisotropy axis perpendicular to the surface, as shown by the two hysteresis loops in **Figure 15a**. The blue hysteresis loop was measured when the external field was applied perpendicular to the BaM film's surface. The red loop was measured when an external field was applied along the BaM film plane. The two loops together confirm the perpendicular orientation of the anisotropy axis of the BaM film.

A Hall bar was fabricated on the Bi_2Se_3/BaM bilayer film. **Figure 15c** shows that, similar to the Hall bar setup of the Pt/BaM experiment discussed in the previous section, the AHE contribution to the Hall bar resistance, R_{AHE}, scales with the

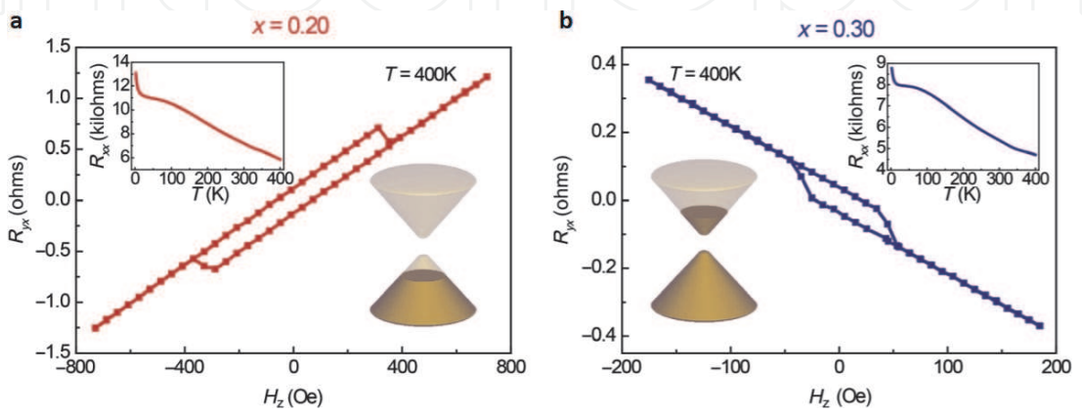

Figure 14.
(a) and (b) Hall traces of TIG/$(Bi_xSb_{1-x})_2 Te_3$ for x = *0.20 and 0.30, respectively. The upper insets show the corresponding temperature dependence of R_{xx}. The lower insets show schematic drawings of the corresponding chemical potential position. Source: [57], p. 2.*

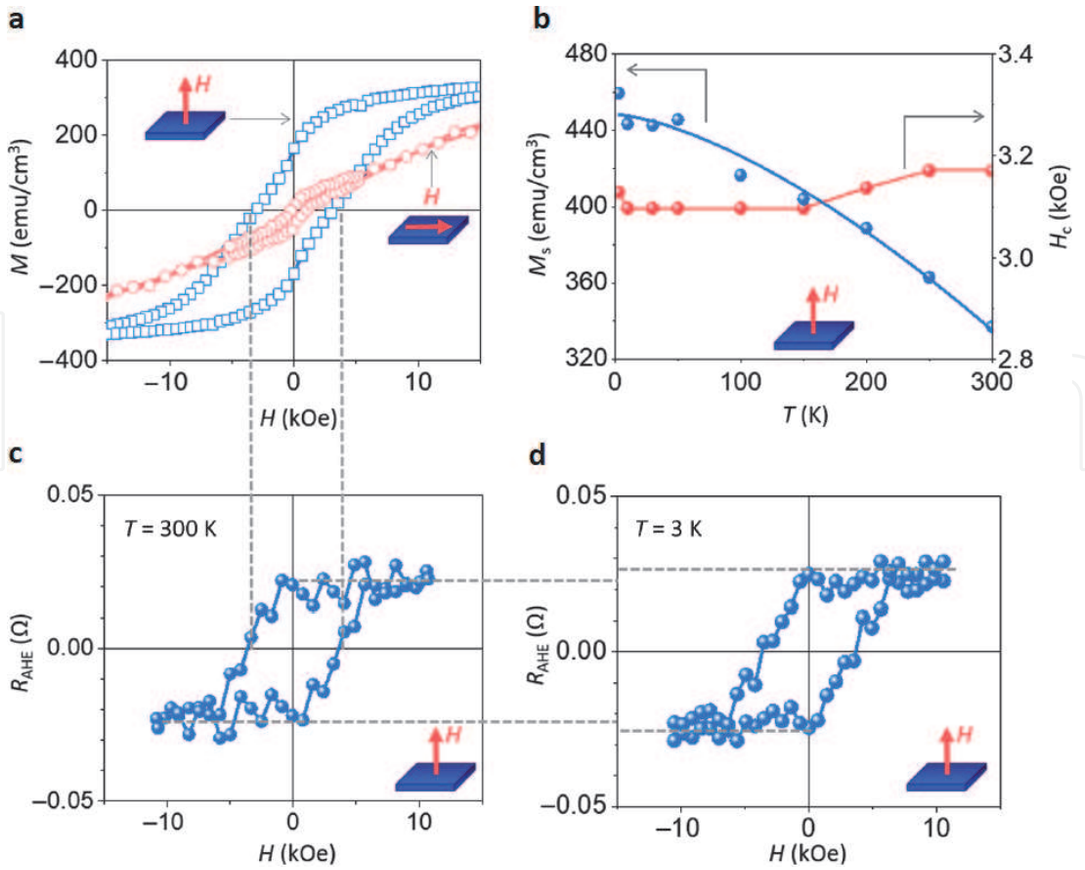

Figure 15.
(a) Magnetization (M) vs. field (H) loops for the $Bi_2Se_3/BaFe_{12}O_{19}$ sample. (b) Saturation magnetization (M_s) and coercive field (H_c) as a function of T. (c) and (d) R_{AHE} vs. field (H) loops measured at T = 300 K and T = 3 K. Source: [10], p. 4.

perpendicular magnetization $M_\perp$ of the BaM film and therefore can be used as an easy way to probe $M_\perp$ of the BaM film during experimentation. While **Figure 15c** shows the R_{AHE} response in room temperature settings, **Figure 15d** shows R_{AHE} when T = 3 K. The figure shows a hysteresis loop that is very close to the one in **Figure 15c**. The hysteresis loop widths are very similar, indicating that the same field strength H is required to saturate the magnetization of the BaM film when T = 3 K and when T = 300 K. The value of R_{AHE} is slightly higher when T = 3 K than when T = 300 K, indicating that the saturation of the BaM film increases slightly as T decreases. The effect of the temperature change on the values of the saturation magnetization of the BaM film and the coercive field required to saturate it are both shown in **Figure 15b**.

Figure 16a shows the SOT switching experiment configuration. An external field H was applied along the x direction to aid in the SOT switching of $M_\perp$ in the BaM film. $M_\perp$ was initially along the positive z direction. **Figure 16b** shows the experimentation results when T = 200 K and H = -15 kOe. The blue data points show the effect of sweeping a DC charge current I_{dc} from positive to negative. When the supplied current was positive, the SOT direction was also in the positive z direction, so we see no change in R_{AHE}. When I_{dc} is <0, however, the SOT direction flips to the negative z direction. When the torque generated by the polarized spin accumulation at the Bi_2Se_3/BaM becomes strong enough, the magnetization within the BaM film switches to the negative z direction, as indicated by the change in R_{AHE} value from positive to negative. Sweeping I_{dc} from negative to positive generates SOT in the +z direction when $I_{dc} > 0$; when the SOT is strong enough, it flips the magnetization of the BaM film again, indicated by the red points in the figure. The result from both cases is a hysteresis loop in R_{AHE} that can be seen in the figure.

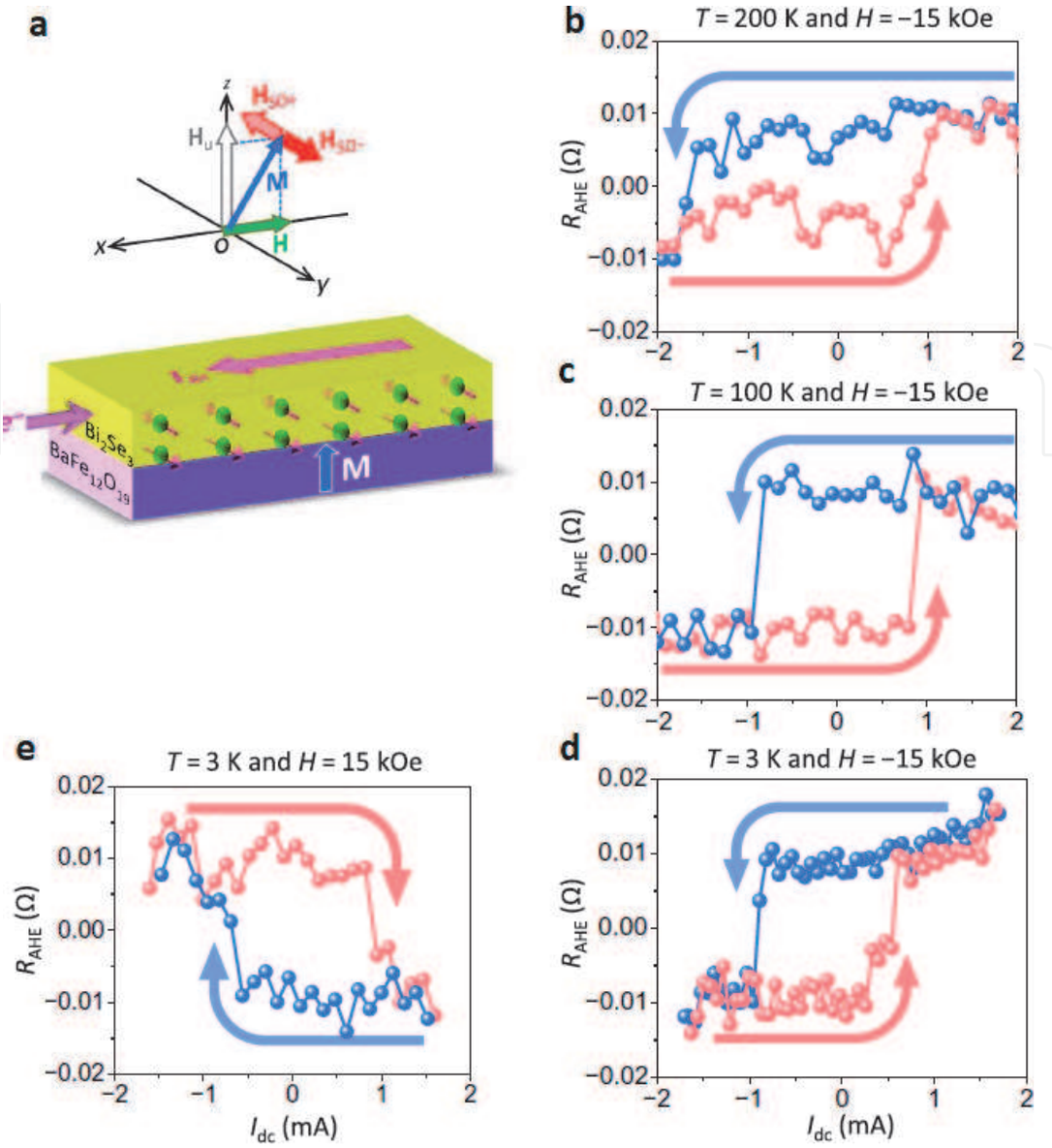

Figure 16.
SOT-induced switching in Bi_2Se_3/BaM. (a) Experimental configuration. (b to e) AHE resistance (R_{AHE}) measured as a function of charge current (I_{dc}) at different fields (H) and temperatures (T), as indicated. The arrows in (b) to (e) indicate the current sweeping directions. Source: [10], p. 5.

Figure 16c, d, and **e** shows the results of the same experiment performed at decreasing temperatures. The figures clearly indicate that the current required for magnetization switching becomes smaller as temperature decreases. This is due to the enhancement of the topological surface states in Bi_2Se_3 as T decreases.

Figure 17 further demonstrates the effect of SOT on the magnetization switching of the BaM film. The experiment was performed at T = 3 K; the external field was applied at 45 degrees angle out of the plane of the film as shown in the inset of the figure. The blue hysteresis loop is the result of applying a negative charge current that generated a SOT acting against *H*. The result is a wider hysteresis loop when compared with the normal hysteresis loop of the BaM film shown in **Figure 15**. This is due to the SOT acting against *H*, therefore hindering the magnetization switching and requiring a stronger external field to switch the magnetization of the BaM film. The red hysteresis loop shows the result of applying a positive charge current, which caused SOT that was in the direction of the external magnetic field, significantly decreasing the switching field required as shown by the much narrower hysteresis loop. This confirms the strength and significance of SOT in TIs and how it can be used to assist in magnetization switching.

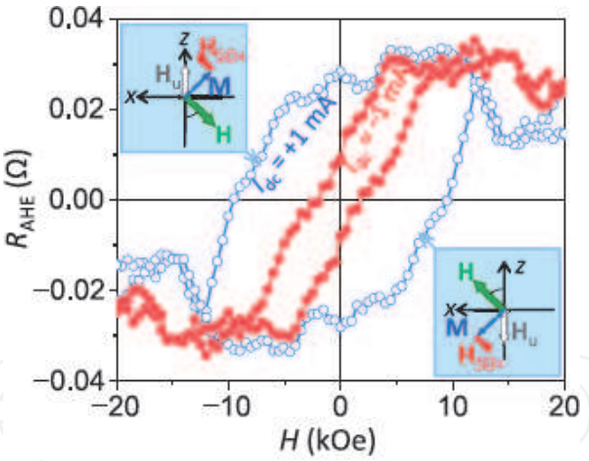

Figure 17.
Effects of I_{dc} on R_{AHE} hysteresis loops at T = 3 K in Bi_2Se_3/BaM. Source: [10], p. 6.

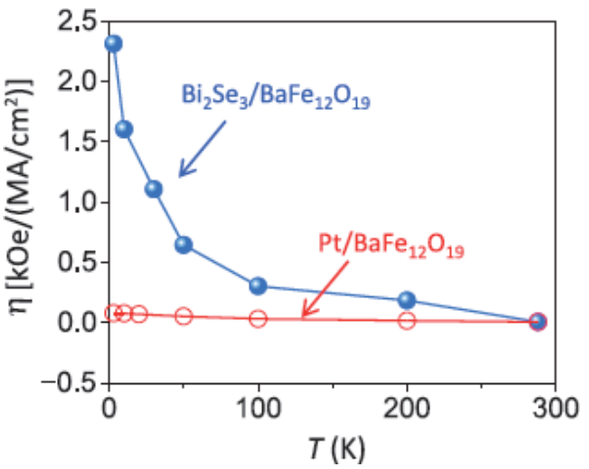

Figure 18.
SOT efficiency (η) as a function of T in Bi_2Se_3/BaM and Pt/BaM. The data were all measured at a field applied at an angle of 45 degrees away from the film normal direction. The data on Pt/BaM were measured with a Hall bar structure that had the same dimension as the Bi_2Se_3/BaM Hall bar. Source: [10], p. 6.

The efficiency of SOT switching can be calculated using the following expression [58]:

$$\eta = \frac{H_{SW}(I_{dc} > 0) - H_{SW}(I_{dc} < 0)}{2|I_{dc}|/(wt)} \quad (6)$$

where H_{SW} is the switching field, w is the Hall bar width, and t is Bi_2Se_3 or Pt thickness. The increase of SOT efficiency as the temperature decreases is demonstrated in **Figure 18**. The blue data points show η of Bi_2Se_3/BaM as a function of temperature. Note that the Debye temperature of Bi_2Se_3 is about 180 K [59]. When T is $>>$ Debye, the efficiency is proportional to T^{-1}, but when the temperature is $<<$ Debye (at T = 100 K), the efficiency is proportional to T^{-5}. Pt/BaM SOT efficiency is also shown as a function of temperature on the same plot (red points). The data show that decreasing the temperature has a negligible effect on the efficiency in Pt/BaM bilayers. The exponential improvement in SOT efficiency of Bi_2Se_3/BaM is caused by the fact that the surface conductance in TIs increases with decreasing temperatures, while the bulk conductance decreases. This means that the decrease in T enhances the TSS in TIs, resulting in a higher charge current to spin current conversion efficiency, increasing the spin polarity in TIs and therefore

generating higher SOT. (All figures, experimentation setup and results were taken from [10] with appropriate permissions).

3.5 Summary and outlook

Magnetic insulators with perpendicular anisotropy have become an important class of materials in the development of spintronic devices. For magnetic domain devices, the low-damping and large anisotropy features can enable high-speed domain-wall motion with a small current threshold, fueling the development of domain-wall memory and logic devices. Moreover, low-damping is significant for SOT oscillator applications, where the current threshold for self-oscillations decreases with damping. Recent experiments show that spin waves can be used to control magnetic domains through spin-orbit torques [60, 61]; this effect can be amplified and become more efficient in magnetic insulators. The strong magnetic anisotropy also allows the engineering of spin-wave dispersion relation without the need for large bias magnetic fields [62]. This will expand the horizon for magnonic and spin-wave devices, allowing the development of new magnon-photon coupling devices for quantum transduction and microwave photonic systems [63, 64].

Author details

Laith Alahmed and Peng Li*
Department of Electrical and Computer Engineering, Auburn University, Auburn, USA

*Address all correspondence to: peng.li@auburn.edu

References

[1] Wolf SA, Awschalom DD, Buhrman RA, Daughton JM, von Molnár S, Roukes ML, et al. Spintronics: A spin-based electronics vision for the future. Science. 2001;**294**(5546): 1488-1495. Available from: https://science.sciencemag.org/content/294/5546/1488

[2] I. Žutić, J. Fabian, and S. Das Sarma, Spintronics: Fundamentals and applications. Reviews of Modern Physics. 2004;**76**:323-410. DOI: 10.1103/RevModPhys.76.323

[3] Fert A. Nobel lecture: Origin, development, and future of spintronics. Reviews of Modern Physics. 2008;**80**: 1517-1530. DOI: 10.1103/RevModPhys.80.1517

[4] Ikeda S, Miura K, Yamamoto H, Mizunuma K, Gan HD, Endo M, et al. A perpendicular-anisotropy CoFeB-MgO magnetic tunnel junction. Nature Materials. 2010;**9**(9):721-724. DOI: 10.1038/nmat2804

[5] Harris VG. Modern microwave ferrites. IEEE Transactions on Magnetics. March 2012;**48**(3):1075-1104

[6] Pullar RC. Hexagonal ferrites: A review of the synthesis, properties and applications of hexaferrite ceramics. Progress in Materials Science. 2012; **57**(7):1191-1334. Available from: http://www.sciencedirect.com/science/article/pii/S0079642512000369

[7] Malkinski L. Advanced Magnetic Materials. Croatia: IntechOpen; 2012

[8] Carosella CA, Chrisey DB, Lubitz P, Horwitz JS, Dorsey P, Seed R, et al. Pulsed laser deposition of epitaxial $BaFe_{12}O_{19}$ thin films. Journal of Applied Physics. 1992;**71**(10):5107-5110. DOI: 10.1063/1.350614

[9] Song Y-Y, Kalarickal S, Patton CE. Optimized pulsed laser deposited barium ferrite thin films with narrow ferromagnetic resonance linewidths. Journal of Applied Physics. 2003;**94**(8): 5103-5110. DOI: 10.1063/1.1608475

[10] Li P, Kally J, Zhang SS-L, Pillsbury T, Ding J, Csaba G, et al. Magnetization switching using topological surface states. Science Advances. 2019;**5**(8). Available from: https://advances.sciencemag.org/content/5/8/eaaw3415

[11] Geiler AL, Yang A, Zuo X, Yoon SD, Chen Y, Harris VG, et al. Atomic scale design and control of cation distribution in hexagonal ferrites. Physical Review Letters. 2008;**101**:067201. DOI: 10.1103/PhysRevLett.101.067201

[12] Mohebbi M, Ebnabbasi K, Vittoria C. In-situ deposition of c-axis oriented barium ferrite films for microwave applications. IEEE Transactions on Magnetics. July 2013; **49**(7):4207-4209

[13] Liu H, Avrutin V, Xiao B, Rowe E, Liu H, Özgür, et al. Epitaxial relationship of mbe grown barium hexaferrite (0001) films on sapphire (0001). Journal of Crystal Growth. 2010;**312**(5):671-675. Available from: http://www.sciencedirect.com/science/article/pii/S0022024809010963

[14] Kranov YA, Abuzir A, Prakash T, McIlroy DN, Yeh WJ. Barium hexaferrite thick films made by liquid phase epitaxy reflow method. IEEE Transactions on Magnetics. October 2006;**42**(10):3338-3340

[15] Yoon SD, Vittoria C. Microwave and magnetic properties of barium hexaferrite films having the c-axis in the film plane by liquid phase epitaxy technique. Journal of Applied Physics. 2003;**93**(10):8597-8599. DOI: 10.1063/1.1557791

[16] Cho TS, Je JH, Noh DY. Formation of crystalline Ba-ferrite phase from -

Fe_2O_3 phase in amorphous precursor. Applied Physics Letters. 2000;**76**(3): 303-305. DOI: 10.1063/1.125727

[17] Zhang X, Meng S, Song D, Zhang Y, Yue Z, Harris VG. Epitaxially grown BaM hexaferrite films having uniaxial axis in the film plane for self-biased devices. Scientific Reports. 2017;**7**(1): 44193. DOI: 10.1038/srep44193

[18] Li P, Ellsworth D, Chang H, Janantha P, Richardson D, Shah F, et al. Generation of pure spin currents via spin Seebeck effect in self-biased hexagonal ferrite thin films. Applied Physics Letters. 2014;**105**(24):242412. DOI: 10.1063/1.4904479

[19] Uchida K, Ishida M, Kikkawa T, Kirihara A, Murakami T, Saitoh E. Longitudinal spin Seebeck effect: From fundamentals to applications. Journal of Physics: Condensed Matter. 2014; **26**(34):343202. DOI: 10.1088

[20] Uchida K, Xiao J, Adachi H, Ohe J, Takahashi S, Ieda J, et al. Spin Seebeck insulator. Nature Materials. 2010; **9**(11):894-897. DOI: 10.1038/nmat2856

[21] Adachi H, Uchida K-I, Saitoh E, Ohe J-I, Takahashi S, Maekawa S. Gigantic enhancement of spin Seebeck effect by phonon drag. Applied Physics Letters. 2010;**97**(25):252506. DOI: 10.1063/ 1.3529944

[22] Uchida K-I, Nonaka T, Ota T, Saitoh E. Longitudinal spin-Seebeck effect in sintered polycrystalline (mn, zn)Fe_2O_4. Applied Physics Letters. 2010;**97**(26):262504. DOI: 10.1063/ 1.3533397

[23] Qu D, Huang SY, Hu J, Wu R, Chien CL, et al. Physical Review Letters. 2013;**110**:067206. DOI: 10.1103/ PhysRevLett.110.067206

[24] Urban R, Woltersdorf G, Heinrich B. Gilbert damping in single and multilayer ultrathin films: Role of interfaces in nonlocal spin dynamics. Physical Review Letters. 2001;**87**:217204. DOI: 10.1103/ PhysRevLett.87.217204

[25] Mizukami S, Ando Y, Miyazaki T. Effect of spin diffusion on gilbert damping for a very thin permalloy layer in Cu/permalloy/Cu/Pt films. Physical Review B. 2002;**66**:104413. DOI: 10.1103/PhysRevB.66.104413

[26] Tserkovnyak Y, Brataas A, Bauer GEW. Enhanced gilbert damping in thin ferromagnetic films. Physical Review Letters. 2002;**88**:117601. DOI: 10.1103/PhysRevLett.88.117601

[27] Heinrich B, Burrowes C, Montoya E, Kardasz B, Girt E, Song Y-Y, et al. Spin pumping at the magnetic insulator (YIG)/normal metal (Au) interfaces. Physical Review Letters. 2011;**107**: 066604. DOI: 10.1103/ PhysRevLett.107.066604

[28] Uchida K, Takahashi S, Harii K, Ieda J, Koshibae W, Ando K, et al. Observation of the spin Seebeck effect. Nature. 2008;**455**(7214):778-781. DOI: 10.1038/nature07321

[29] Uchida K, Ota T, Harii K, Takahashi S, Maekawa S, Fujikawa Y, et al. Spin-Seebeck effects in $Ni_{81}Fe_{19}$/Pt films. Solid State Communications. 150, 2010;**11**:524-528. Spin Caloritronics. Available from: http://www.sciencedirect.com/science/article/pii/S003810980900698X

[30] Jaworski CM, Yang J, Mack S, Awschalom DD, Heremans JP, Myers RC. Observation of the spin-Seebeck effect in a ferromagnetic semiconductor. Nature Materials. 2010; **9**(11):898-903. DOI: 10.1038/nmat2860

[31] Jaworski CM, Myers RC, Johnston-Halperin E, Heremans JP. Giant spin Seebeck effect in a non-magnetic material. Nature. 2012;**487**(7406): 210-213. DOI: 10.1038/nature11221

[32] Meier D, Kuschel T, Shen L, Gupta A, Kikkawa T, Uchida K, et al. Thermally driven spin and charge currents in thin $NiFe_2O_4$/Pt films. Physical Review B. February 2013;**87**:054421. DOI: 10.1103/PhysRevB.87.054421

[33] Ramos R, Kikkawa T, Uchida K, Adachi H, Lucas I, Aguirre MH, et al. Observation of the spin Seebeck effect in epitaxial fe3o4 thin films. Applied Physics Letters. 2013;**102**(7):072413. DOI: 10.1063/1.4793486

[34] Ashcroft N, Mermin D. Solid State Physics. Belmont, California: Brooks/Cole; 1976

[35] Bosu S, Sakuraba Y, Uchida K, Saito K, Ota T, Saitoh E, et al. Spin Seebeck effect in thin films of the heusler compound Co_2MnSi. Physical Review B. June 2011;**83**:224401. DOI: 10.1103/PhysRevB.83.224401

[36] Slonczewski JC. Conductance and exchange coupling of two ferromagnets separated by a tunneling barrier. Physical Review B. April 1989;**39**: 6995-7002. DOI: 10.1103/PhysRevB.39.6995

[37] Jedema FJ, Filip AT, van Wees BJ. Electrical spin injection and accumulation at room temperature in an all-metal mesoscopic spin valve. Nature. 2001; **410**(6826):345-348. DOI: 10.1038/35066533

[38] Maekawa S, Adachi H, Uchida K-I, Ieda J, Saitoh E. Spin current: Experimental and theoretical aspects. Journal of the Physical Society of Japan. 2013;**82**(10):102002. DOI: 10.7566/JPSJ.82.102002

[39] Uchida K, Ota T, Adachi H, Xiao J, Nonaka T, Kajiwara Y, et al. Thermal spin pumping and magnon-phonon-mediated spin-Seebeck effect. Journal of Applied Physics. 2012;**111**(10):103903. DOI: 10.1063/1.4716012

[40] Uchida K-I, Adachi H, Ota T, Nakayama H, Maekawa S, Saitoh E. Observation of longitudinal spin-Seebeck effect in magnetic insulators. Applied Physics Letters. 2010;**97**(17): 172505. DOI: 10.1063/1.3507386

[41] Berger L. Application of the side-jump model to the Hall effect and Nernst effect in ferromagnets. Physical Review B. 1972;**5**:1862-1870. DOI: 10.1103/PhysRevB.5.1862

[42] Miyasato T, Abe N, Fujii T, Asamitsu A, Onoda S, Onose Y, et al. Crossover behavior of the anomalous Hall effect and anomalous Nernst effect in itinerant ferromagnets. Physical Review Letters. August 2007;**99**:086602. DOI: 10.1103/PhysRevLett.99.086602

[43] Saitoh E, Ueda M, Miyajima H, Tatara G. Conversion of spin current into charge current at room temperature: Inverse spin-Hall effect. Applied Physics Letters. 2006;**88**(18): 182509. DOI: 10.1063/1.2199473

[44] Kimura T, Otani Y, Sato T, Takahashi S, Maekawa S. Room-temperature reversible spin Hall effect. Physical Review Letters. 2007;**98**:156601. DOI: 10.1103/PhysRevLett.98.156601

[45] Azevedo A, Vilela Leão LH, Rodriguez-Suarez RL, Oliveira AB, Rezende SM. dc effect in ferromagnetic resonance: Evidence of the spin-pumping effect? Journal of Applied Physics. 2005; **97**(10):10C715. DOI: 10.1063/1.1855251

[46] Valenzuela SO, Tinkham M. Direct electronic measurement of the spin Hall effect. Nature. 2006;**442**(7099):176-179. DOI: 10.1038/nature04937

[47] Costache MV, Sladkov M, Watts SM, van der Wal CH, van Wees BJ. Electrical detection of spin pumping due to the processing magnetization of a single ferromagnet. Physical Review Letters. 2006;**97**:216603. DOI: 10.1103/PhysRevLett.97.216603

[48] Ellsworth D, Lu L, Lan J, Chang H, Li P, Wang Z, et al. Photo-spin-voltaic

effect. Nature Physics. 2016;**12**(9): 861-866. DOI: 10.1038/nphys3738

[49] Chen Y-J, Huang S-Y. Light-induced thermal spin current. Physical Review B. 2019;**99**:094426. DOI: 10.1103/PhysRevB.99.094426

[50] Kattel S, Murphy JR, Ellsworth D, Ding J, Liu T, Li P, et al. Broadband optical detection using the spin Seebeck effect. Physical Review Applied. 2019; **12**:034047. DOI: 10.1103/PhysRevApplied.12.034047

[51] Li P, Liu T, Chang H, Kalitsov A, Zhang W, Csaba G, et al. Spin-orbit torque-assisted switching in magnetic insulator thin films with perpendicular magnetic anisotropy. Nature Communications. 2016;**7**(1):12688. DOI: 10.1038/ncomms12688

[52] Zhang J, Velev JP, Dang X, Tsymbal EY. Band structure and spin texture of $Bi_2Se_3$3*d* ferromagnetic metal interface. Physical Review B. 2016;**94**: 014435. DOI: 10.1103/PhysRevB.94.014435

[53] Avci CO, Quindeau A, Pai C-F, Mann M, Caretta L, Tang AS, et al. Current-induced switching in a magnetic insulator. Nature Materials. 2017;**16**(3): 309-314. DOI: 10.1038/nmat4812

[54] Hoffmann A. Spin Hall effects in metals. IEEE Transactions on Magnetics. 2013;**49**(10):5172-5193

[55] Zhang S. Spin Hall effect in the presence of spin diffusion. Physical Review Letters. 2000;**85**:393-396. DOI: 10.1103/PhysRevLett.85.393

[56] Day C. Two groups observe the spin Hall effect in semiconductors. Physics Today. 2005;**58**(2):17-19. DOI: 10.1063/1.1897513

[57] Tang C, Chang C-Z, Zhao G, Liu Y, Jiang Z, Liu C-X, et al. Above 400-k robust perpendicular ferromagnetic phase in a topological insulator. Science Advances. 2017;**3**:6. Available from: https://advances.sciencemag.org/content/3/6/e1700307

[58] Khang NHD, Ueda Y, Hai PN. A conductive topological insulator with large spin Hall effect for ultralow power spin-orbit torque switching. Nature Materials. 2018;**17**(9):808-813. DOI: 10.1038/s41563-018-0137-y

[59] Chen X, Zhou HD, Kiswandhi A, Miotkowski I, Chen YP, Sharma PA, et al. Thermal expansion coefficients of Bi_2Se_3 and Sb_2Te_3 crystals from 10 k to 270 k. Applied Physics Letters. 2011; **99**(26):261912. DOI: 10.1063/1.3672198

[60] Wang Y, Zhu D, Yang Y, Lee K, Mishra R, Go G, et al. Magnetization switching by magnon-mediated spin torque through an antiferromagnetic insulator. Science. 2019;**366**(6469):1125. Available from: http://science.sciencemag.org/content/366/6469/1125.abstract

[61] Han J, Zhang P, Hou JT, Siddiqui SA, Liu L. Mutual control of coherent spin waves and magnetic domain walls in a magnonic device. Science. 2019;**366**(6469):1121-1125. Available from: https://science.sciencemag.org/content/366/6469/1121

[62] Soumah L, Beaulieu N, Qassym L, Carrétéro C, Jacquet E, Lebourgeois R, et al. Ultra-low damping insulating magnetic thin films get perpendicular. Nature Communications. 2018;**9**(1): 3355. DOI: 10.1038/s41467-018-05732-1

[63] Hou JT, Liu L. Strong coupling between microwave photons and nanomagnet magnons. Physical Review Letters. 2019;**123**:107702. DOI: 10.1103/PhysRevLett.123.107702

[64] Li Y, Polakovic T, Wang Y-L, Xu J, Lendinez S, Zhang Z, et al. Strong coupling between magnons and microwave photons in on-chip ferromagnet-superconductor thin-film devices. Physical Review Letters. 2019; **123**:107701. DOI: 10.1103/PhysRevLett.123.107701